Design and Operation of an Annular Helicon Plasma Source

Masayuki Yano[*], Doug Palmer[†], Logan Williams[‡], and Mitchell L. R. Walker[§]
High-Power Electric Propulsion Laboratory, Georgia Institute of Technology, Atlanta, GA 30332

An annular helicon plasma source for the ionization stage of a two-stage Hall effect thruster is considered. The magnetic and electric field structures in the plasma source are computed considering classical helicon wave and Trivelpiece-Gould wave. The antenna coupling and power deposition mechanism model is developed to determine the effective antenna geometry. Methodology for selecting the antenna power, frequency, and applied magnetic field strength is presented. Using the theoretical model, the annular helicon source compatible with a 5-kW Hall thruster is sized and built.

Nomenclature

$\mathbf{B}$	=	perturbed magnetic field vector
B_r, B_θ, B_z	=	components of the perturbed magnetic field vector
c	=	speed of light
e	=	charge of an electron
$\mathbf{E}$	=	perturbed electric field vector
E_r, E_θ, E_z	=	components of the perturbed electric field vector
$\mathbf{F}$	=	arbitrary vector field quantity
F_r, F_θ, F_z	=	components of an arbitrary vector field
$F_j(r,m,k)$	=	arbitrary quantity in Fourier space
$f_j(r,m,k)$	=	arbitrary quantity in physical space
HET	=	Hall effect thruster
k	=	wave number
k_0	=	wave number in free space
I_0	=	magnitude of antenna current
I_n, K_n	=	modified Bessel function of the first and second kind (order n)
$\mathbf{j}$	=	perturbed current vector
j_r, j_θ, j_z	=	components of the perturbed current vector
J_n, Y_n	=	Bessel function of the first and second kind (order n)
$\mathbf{K}$	=	surface current density of antenna
K_θ, K_z	=	components of antenna surface current density
m	=	wave mode number
m_e	=	mass of an electron
n	=	local plasma number density
n_0	=	peak plasma number density
n_a	=	neutral number density
p_m, s_m, q_m, ρ_m	=	geometric functions
P_p	=	power deposited into plasma
P_s	=	spectral plasma power
P_r	=	power absorbed by an infinitely thin shell
Q_{ei}	=	electron-ion momentum collision cross section
r, θ, z	=	radial, azimuthal, and axial position
$\hat{r}, \hat{\theta}, \hat{z}$	=	radial, azimuthal, and axial coordinate unit vectors

[*]Undergraduate Student Researcher, Aerospace Engineering, 270 Ferst Drive, Atlanta, GA 30332, Member AIAA
[†] Graduate Student Researcher, Aerospace Engineering, 270 Ferst Drive, Atlanta, GA 30332, Member AIAA.
[‡] Graduate Student Researcher, Aerospace Engineering, 270 Ferst Drive, Atlanta, GA 30332, Member AIAA.
[§] Assistant Professor, Aerospace Engineering, 270 Ferst Drive, Atlanta, GA, 30332, Member AIAA.

S, P, D	=	entries of the effective dielectric constant tensor
T	=	transverse wave number
T_0	=	traverse wave number in free space
$\mathbf{v}$	=	electron velocity
V_D	=	discharge voltage
V_{nc}	=	neutralizer coupling voltage
β	=	total wave number
δ	=	collision parameter
ε	=	ionization cost
ε_0	=	permittivity of free space
ε_e	=	electron energy
$\underline{\varepsilon}$	=	plasma dielectric tensor
η_u	=	propellant utilization efficiency
λ_D	=	Debye length
μ_0	=	permeability of free space
γ	=	plume divergence coefficient
υ	=	collision rate
υ_{ei}	=	electron-ion collision rate
υ_{ea}	=	electron-atom collision rate
ω	=	wave angular frequency
ω_{ce}, ω_{ci}	=	electron and ion cyclotron frequency
ω_{pe}, ω_{pi}	=	electron and ion plasma frequency

I. Introduction

Two-stage Hall effect thrusters (HETs), which decouple the ionization stage from the acceleration stage, could achieve a higher efficiency in high-thrust, low-Isp operation than single-stage HETs. The efficiency of a single-stage HET, which is defined as a ratio of the thrust power to the input power, is expressed as[1]

$$\eta = \frac{P_{thrust}}{P_{input}} = \frac{\eta_u \gamma^2}{1 + (\varepsilon + V_{nc})/V_D}, \tag{1}$$

where η_u is the propellant utilization efficiency, γ is the plume divergence coefficient, ε is the ionization cost, V_{nc} is the neutralizer coupling voltage, and V_D is the discharge voltage. High-thrust operation requires high mass flow at a low discharge voltage. However, Eq. (1) shows that the efficiency of thruster decreases at a low discharge voltage because a large fraction of energy is spent on ionization instead of acceleration. A solution to the problem is to replace the DC electron bombardment ionization stage with an efficient ionization source and decouple the ionization and acceleration mechanisms.[2] Two-stage HETs, which have separate ionization and acceleration stages, have been investigated in the past[3,4], but a helicon source has never been used as the ionization stage.

A helicon plasma source is a high density, high efficiency plasma source that sustains steady plasma production through absorption and propagation of helicon waves.[5,6] The wave is launched by applying an axial magnetic field, while coupling an RF antenna to the plasma column. To date, helicon waves have only been excited in cylindrical sources. A cylindrical source is not suitable for the ionization stage of a HET because guiding cylindrical plasma into an annular channel would result in a large plasma loss. However, if helicon plasma can be excited in a coaxial configuration, the source can directly feed high-density plasma into the acceleration stage of a HET and other coaxial accelerators.[7] The existence of annularly-bounded helicon waves in theory has been discussed previously.[8,9] This article presents the theory of annularly-bounded helicon plasmas, methods used for sizing the device, and preliminary experimental results.

II. Theory and Model

Figure 1 shows the cross-sectional view of the annular helicon model configuration. As the figure shows, the plasma is bounded by insulating material at $r = b$ and $r = c$, where r is the radius from the centerline of the device. Two half-helical antennas are located at $r = a$ and $r = d$. The device is surrounded by a conducting cylinder at $r = e$, which corresponds to the vacuum chamber wall in experiments. Typically, the conducting wall is located sufficiently far from the device that the choice of e has negligible effect on the plasma. The generalized dispersion relation for annularly-bounded helicon plasma is obtained from Maxwell's equations and the electron fluid equation of motion. For simplicity, the perturbation of the form

$$\mathbf{F}(r,\theta,z,t) = \left(F_r(r)\hat{r} + F_\theta(r)\hat{\theta} + F_z(r)\hat{z}\right)\exp(i(m\theta + kz - \omega t)) \quad (2)$$

is considered, where $\mathbf{F}$ is a vector quantity (e.g. magnetic field), F_r, F_θ, and F_z are the components of $\mathbf{F}$, m is the mode number, k is the parallel wave number, and ω is the angular frequency of the wave.
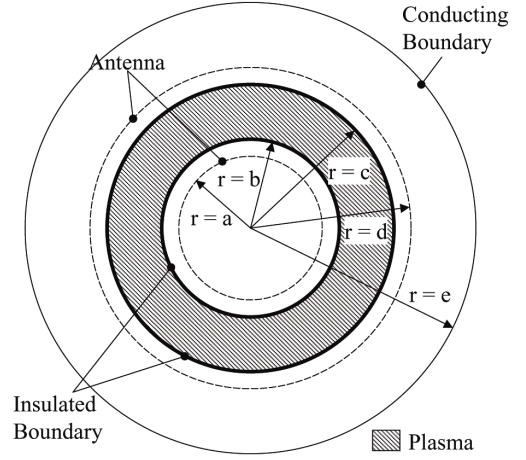
Figure 1. The cross-sectional view of the annular-helicon model.

A. Plasma Basis Functions

With the perturbation of the form defined above, the Maxwell's equations are expressed as

$$\nabla \cdot \mathbf{B} = 0 \tag{3}$$

$$\nabla \times \mathbf{E} = i\omega\mathbf{B} \tag{4}$$

$$\nabla \times \mathbf{B} = \mu_0\left(\mathbf{j} - i\omega\varepsilon_0\mathbf{E}\right), \tag{5}$$

and the linearized fluid equation of motion for species s is

$$-i\omega m_s \mathbf{v} = -e\left(\mathbf{E} + \mathbf{v} \times \mathbf{B_0}\right) - m_s \upsilon\mathbf{v} \tag{6}$$

where $\mathbf{B}$ is the perturbation in magnetic field, $\mathbf{E}$ is the perturbation in electric field, $\mathbf{j}$ is the perturbation in the current, μ_0 is the permeability of free space, ε_0 is the permittivity of free space, m_e is the electron mass, $\mathbf{v}$ is the electron velocity, e is the electron charge, $\mathbf{B_0} = B_0\hat{z}$ is the applied magnetic field, and υ is the collision rate. The magnetic viscosity term and the pressure term are neglected from Eq. (6) because these terms are not important in helicon wave propagation.[10] Only the electron and one species of ion is considered throughout this paper, but the result can be generalized for plasma with multiple ion species. For waves in cold plasmas, Eq. (5) can be expressed in terms of the effective dielectric constant of plasma $\underline{\varepsilon}$ using Eq. (6), *i.e.*[11]

$$\nabla \times \mathbf{B} = -i\mu_0\omega\underline{\varepsilon}\mathbf{E}, \tag{7}$$

where $\underline{\varepsilon}$ is defined as

$$\underline{\varepsilon} \equiv \varepsilon_0\begin{bmatrix} S & -iD & 0 \\ iD & S & 0 \\ 0 & 0 & P \end{bmatrix}, \tag{8}$$

with

$$S, D \equiv (R \pm L)/2,$$ (9)

$$R, L \equiv 1 - \frac{\omega_{pe}^2}{\delta_e^2 \omega^2}\left(\frac{1}{1 \mp \omega_{ce}/(\delta_e \omega)}\right) - \frac{\omega_{pi}^2}{\delta_i^2 \omega^2}\left(\frac{1}{1 \pm \omega_{ci}/(\delta_i \omega)}\right),$$ (10)

$$P \equiv 1 - \frac{\omega_{pe}^2}{\delta_e^2 \omega^2} - \frac{\omega_{pi}^2}{\delta_i^2 \omega^2},$$ (11)

$$\delta_e = 1 + i\frac{\upsilon_{ei} + \upsilon_{ea}}{\omega},$$ (12)

$$\delta_i = 1 + i\frac{\upsilon_{ei}}{\omega},$$ (13)

where ω_{pe} is the electron plasma frequency, ω_{ce} is the electron cyclotron frequency, ω_{pi} is the ion plasma frequency, ω_{ci} is the ion cyclotron frequency, and δ is the collision parameter. The characteristic frequencies are defined as

$$\omega_{pe,pi}^2 \equiv \frac{ne^2}{\varepsilon_0 m_{e,i}},$$ (14)

$$\omega_{ce,ci} \equiv \frac{eB_0}{m_{e,i}},$$ (15)

where m_e is the mass of an electron, m_i is the mass of an ion, and n is the plasma number density. A combination of Eqs. (4) and (7) yields a set of four ordinary differential equations, which defines the electric and magnetic fields in plasma,[12] i.e.

$$\frac{\partial E_\theta}{\partial r} = -\frac{1}{r}\left(\frac{D}{S}m+1\right)E_\theta + i\frac{1}{S}\frac{m}{r}\frac{kc^2}{\omega}B_\theta + i\omega\left(1 - \frac{1}{S}\frac{m^2}{r^2 k_0^2}\right)B_z$$ (16)

$$\frac{\partial E_z}{\partial r} = -\frac{D}{S}kE_\theta - i\omega\left(1 - \frac{1}{S}\frac{k^2}{k_0^2}\right)B_\theta - i\frac{1}{S}\frac{m}{r}\frac{kc^2}{\omega}B_z$$ (17)

$$\frac{\partial B_\theta}{\partial r} = -\frac{im}{r}\frac{k}{\omega}E_\theta - i\frac{\omega}{c^2}\left(P - \frac{m^2}{r^2 k^2}\right)E_z - \frac{1}{r}B_\theta$$ (18)

$$\frac{\partial B_z}{\partial r} = -i\frac{1}{\omega}\left(k^2 - k_0^2 S + \frac{D^2}{S}k_0^2\right)E_\theta + i\frac{k}{\omega}\frac{m}{r}E_z - \frac{D}{S}kB_\theta + \frac{D}{S}\frac{m}{r}B_z,$$ (19)

where $k_0 = \omega/c$ is the wave number in free space and S, D, and P are the components of the plasma dielectric tensor defined in Eqs. (9) - (11). Equations (16) - (19) form a closed set, which solves for azimuthal and axial wave fields. The radial components of the wave field are obtained from

$$B_r = \frac{m}{\omega r}E_z - \frac{k}{\omega}E_\theta,$$ (20)

$$E_r = i\frac{D}{S}E_\theta + \frac{1}{S}\frac{kc^2}{\omega}B_\theta - \frac{1}{S}\frac{m}{r}\frac{c^2}{\omega}B_z.$$ (21)

In order to compute these basis functions, the initial condition is specified at the inner wall ($r = b$) based on the result for the collisionless uniform-density case, and the set of ODE's are numerically integrated outward. For the uniform density-case, there are helicon and Trivelpiece-Gould (TG) solutions with two distinct Bessel functions. Thus, there are a total of four basis functions. The magnetic field is expressed in terms of the Bessel functions as

$$B_{r,j} = A_j \left[(\beta_j + k) J_{m-1}(T_j r) + (\beta_j - k) J_{m+1}(T_j r) \right] \\ + B_j \left[(\beta_j + k) Y_{m-1}(T_j r) + (\beta_j - k) Y_{m+1}(T_j r) \right], \tag{22}$$

$$B_{\theta,j} = i A_j \left[(\beta_j + k) J_{m-1}(T_j r) - (\beta_j - k) J_{m+1}(T_j r) \right] \\ + i B_j \left[(\beta_j + k) Y_{m-1}(T_j r) - (\beta_j - k) Y_{m+1}(T_j r) \right], \tag{23}$$

$$B_{z,j} = -2i A_j T_j J_m(T_j r) - 2i B_j T_j Y_m(T_j r), \tag{24}$$

where J_m and Y_m are the Bessel functions of the first and second kind, respectively, $T_j^2 = \beta_j^2 - k^2$, and β_j is a solution to

$$\left(\frac{\omega}{\omega_{ce}} \right)^2 \beta_j^2 - k \beta_j + \frac{\omega n_0 \mu_0 e}{B_0} = 0. \tag{25}$$

The subscript $j = 1$ corresponds to helicon branch of the solution, and $j = 2$ corresponds to TG branch of the solution. Note, β is the total wave number, and T is the transverse wave number. In a cylindrical case, only Bessel function of first kind is allowed because Bessel function of second kind is singular at the origin[5]; however, both J_m and Y_m basis functions are valid in an annular case because the plasma region does not include the origin. Although the effect of finite electron mass was neglected in earlier analyses,[5,8] the importance of the finite mass effect has been confirmed.[9,10] In particular, finite electron mass introduces a Trivelpiece-Gould (TG) wave, and the solution becomes a superposition of the classical helicon wave and the TG wave. In the absence of collision and displacement current,[5] the current is parallel to the magnetic field. Thus, axial component of the electric field is

$$E_z = -i \frac{\omega}{\varepsilon_0 \omega_{pe}^2} j_z = -i \frac{\omega}{\varepsilon_0 \omega_{pe}^2} \frac{\beta_j}{\mu_0} B_z. \tag{26}$$

The radial and azimuthal components of electric field is obtained from Eq. (4), *i.e.*

$$E_\theta = \frac{m}{rk} E_z - \frac{\omega}{k} B_r, \tag{27}$$

$$E_r = -\frac{i}{k} E_z' + \frac{\omega}{k} B_\theta. \tag{28}$$

After obtaining the basis for electric and magnetic fields using Eqs. (16) - (21), the current is obtained from the plasma dielectric tensor. The total current, which is the sum of the real and displacement current, is equal to

$$\mathbf{J} = -i\omega \underline{\varepsilon} \mathbf{E}, \tag{29}$$

where $\underline{\varepsilon}$ is the dielectric tensor defined by Eq. (8). Similarly, the real current is expressed as

$$\mathbf{J} = -i\omega (\underline{\varepsilon} - \mathbf{I}) \mathbf{E}, \tag{30}$$

where $\mathbf{I}$ is an identity matrix.

The evaluation of Eqs. (12) and (13) requires the electron-neutral and electron-ion collision frequencies. Thus, the collisional cross section of each collision type must be approximated. The convolution of electron-neutral cross section[13] with Mawellian distribution with the mean kinetic energy of 3 eV yields the effective electron-neutral cross section. The electron-ion collision cross section is approximated based on[13]

$$Q_{ei} = \frac{\pi e^4}{(4\pi\varepsilon_0)^2 \varepsilon^2} \ln\left(\frac{8\pi\varepsilon_0 \lambda_D \varepsilon}{e^2}\right),\tag{31}$$

where ε is the kinetic energy of electron and λ_D is the Debye length.

B. Vacuum Basis Functions

As helicon sources uses RF antennas located outside of the plasma region to couple to the plasma, the electric and magnetic field in the vacuum region must be also evaluated to compute the wave field in the plasma. A basis function for the vacuum region is obtained in a similar manner as the plasma basis functions. In the absence of current, the combination of Eq. (3) - (5) yields

$$\nabla^2 \mathbf{B} + k_0 \mathbf{B} = 0,\tag{32}$$

where $k_0 = \omega/c$ and c is the speed of light. A combination of Eq. (32) and the no magnetic divergence condition yields four linearly independent solutions. The general solution is of the form,

$$B_r = C_1 I'_m(T_0 r) + C_2 \frac{m}{T_0 r} I_m(T_0 r) + C_3 K'_m(T_0 r) + C_4 \frac{m}{T_0 r} K_m(T_0 r)\tag{33}$$

$$B_\theta = i\left[C_1 \frac{m}{T_0 r} I_m(Tr) + C_2 I'_m(T_0 r) + C_3 \frac{m}{T_0 r} K_m(T_0 r) - C_4 K'_m(T_0 r)\right]\tag{34}$$

$$B_z = i\frac{T}{k}\left[C_1 I_m(T_0 r) + C_3 K_m(T_0 r)\right],\tag{35}$$

where $T_0^2 = k_0^2 - k^2$ and I_m and K_m are the modified Bessel functions of first and second kind, respectively. The prime ($'$) is derivative with respect to the argument of Bessel functions $T_0 r$, and not r. The derivatives of Bessel functions are evaluated using the recursive relationships. Equation (5) yields the electric field in the vacuum regions, i.e.

$$E_r = \frac{c^2}{\omega}\left[-\frac{m}{r}B_z + kB_\theta\right],\tag{36}$$

$$E_\theta = \frac{c^2}{\omega}\left[-kB_r - iB'_z\right],\tag{37}$$

$$E_z = \frac{c^2}{\omega r}\left[iB_\theta + irB'_\theta + mB_r\right] = -C_2 \frac{T\omega}{k_0^2} I_m(T_0 r) - C_4 \frac{T\omega}{k_0^2} K_m(T_0 r).\tag{38}$$

It is important to note that the basis for the axial magnetic and axial electric field in the vacuum region is simply I_m and K_m. These basis expressions greatly simplify boundary condition matching. As the boundary condition matching also requires azimuthal component of the fields, it is useful to define E_θ and B_θ in terms of E_z and B_z. A combination of Eqs. (4) and (5) yields

$$E_\theta = \frac{mk}{T_0^2 r} E_z + i \frac{\omega}{T_0^2} \frac{\partial B_z}{\partial r}, \tag{39}$$

$$B_\theta = \frac{mk}{T_0^2 r} B_z - i \frac{k_0^2}{\omega T_0^2} \frac{\partial E_z}{\partial r}. \tag{40}$$

C. Boundary Conditions

After obtaining the basis functions, the boundary conditions are applied to obtain the unknown coefficients. There are a total of 18 unknown coefficients. Each of the five regions has four basis function, which results in 20 unknown coefficients. However, two of the vacuum basis functions are singular at the origin, so this reduces the total number of unknowns to 18. The tangential electric field (E_θ and E_z) is continuous at each of the five boundaries, which gives 10 boundary conditions. The tangential magnetic field (B_θ and B_z) is continuous at plasma interface, but goes through a jump across the antenna according to

$$B_\theta^{out} - B_\theta^{in} = \mu_0 K_z \tag{41}$$

$$B_z^{out} - B_z^{in} = -\mu_0 K_\theta, \tag{42}$$

where K_z and K_θ are the axial and azimuthal components of the antenna current. For each component of F_i of any field in plasma (*i.e.* **E**, **B**, and **J**), the solution is expressed as a linear combination of basis functions, *i.e.*

$$F_j(r) = P_1 f_{1,j}(r) + P_2 f_{2,j}(r) + P_3 f_{3,j}(r) + P_4 f_{4,j}(r), \tag{43}$$

where $f_{i,j}$ is the *i*-th basis function of quantity f in the *j*-th coordinate. For example, the radial electric field is expressed as

$$E_r(r) = P_1 e_{1,r}(r) + P_2 e_{2,r}(r) + P_3 e_{3,r}(r) + P_4 e_{4,r}(r), \tag{44}$$

where $e_{i,r}$ are the four independent solutions to Eqs. (16) - (21). The coefficients P_i is readily found by solving a 4×4 linear system defined by

$$\begin{bmatrix} A_1 & A_2 & A_3 & A_4 \\ B_1 & B_2 & B_3 & B_4 \\ C_1 & C_2 & C_3 & C_4 \\ D_1 & D_2 & D_3 & D_4 \end{bmatrix} \begin{bmatrix} P_1 \\ P_2 \\ P_3 \\ P_4 \end{bmatrix} = \begin{bmatrix} -i \dfrac{a}{b} \dfrac{k}{T_0} I'_m(T_0 a) \mu_0 K_{1,\theta} \\ -i \dfrac{m}{b} \dfrac{k_0^2}{T_0^2} I_m(T_0 a) K_{1,\theta} \\ i \dfrac{d}{c} \dfrac{k}{T_0} s_m \mu_0 K_{2,\theta} \\ i \dfrac{m}{c} \dfrac{k_0^2}{T_0^2} \rho_m K_{2,\theta} \end{bmatrix}, \tag{45}$$

where

$$A_n = b_{n,r}(b) + i \frac{k}{T_0} b_{n,z}(b) + \frac{m}{b T_0^2} \omega \mu_0 \varepsilon_0 e_{n,z}(b), \tag{46}$$

$$B_n = j_{n,r}(b) + i \frac{m}{b} \frac{k_0^2}{T_0^2} \frac{1}{\mu_0} b_{n,z}(b) + \omega \varepsilon_0 \left(\frac{k}{T_0} e_{n,z}(b) - i e_{n,r}(b) \right), \tag{47}$$

$$C_n = b_{n,r}(c) + i\frac{k}{T_0} p_m b_{n,z}(c) + \frac{m}{cT_0^2}\omega\mu_0\varepsilon_0 e_{n,z}(c), \tag{48}$$

$$D_n = j_{n,r}(c) + i\frac{m}{c}\frac{k_0^2}{T_0^2}\frac{1}{\mu_0} b_{n,z}(c) + \omega\varepsilon_0\left(\frac{k}{T_0} q_m e_{n,z}(c) - ie_{n,r}(c)\right), \tag{49}$$

and

$$p_m = \frac{K'_m(T_0 c)I'_m(T_0 e) - K'_m(T_0 e)I'_m(T_0 c)}{K_m(T_0 c)I'_m(T_0 e) - K'_m(T_0 e)I_m(T_0 c)}, \tag{50}$$

$$s_m = \frac{K'_m(T_0 d)I'_m(T_0 e) - K'_m(T_0 e)I'_m(T_0 d)}{K_m(T_0 c)I'_m(T_0 e) - K'_m(T_0 e)I_m(T_0 c)}, \tag{51}$$

$$q_m = \frac{K'_m(T_0 c)I_m(T_0 e) - K_m(T_0 e)I'_m(T_0 c)}{K_m(T_0 c)I_m(T_0 e) - K_m(T_0 e)I_m(T_0 c)}, \tag{52}$$

$$\rho_m = \frac{K_m(T_0 d)I_m(T_0 e) - K_m(T_0 e)I_m(T_0 d)}{K_m(T_0 c)I_m(T_0 e) - K_m(T_0 e)I_m(T_0 c)}, \tag{53}$$

where a, b, c, d, and e correspond to the radii described in Figure 1. Note, the condition imposed at the outer boundary is identical to the relationship previously presented for the cylindrical source.[14, 12]

D. Antenna Coupling

Assuming the plasma is uniform in axial and azimuthal directions, a Fourier transform is applied in these directions to express the antenna as a cylindrical current sheet. Following the convention introduced by Chen, each component of a vector $\mathbf{f}$ is expressed as[14]

$$f_j(r,\theta,z) = \frac{1}{2\pi}\int_{-\infty}^{\infty}\sum_{m=-\infty}^{\infty} F_j(r,m,k)\exp(i(m\theta + kz))dk \tag{54}$$

where

$$F_j(r,m,k) = \frac{1}{2\pi}\int_{-\infty}^{\infty}\int_0^{2\pi} f_j(r,\theta,z)\exp(-i(m\theta + kz))d\theta dz . \tag{55}$$

f_j is a quantity in physical space, and F_j is a quantity in Fourier domain. In the Fourier domain, the current through a half-helical antenna is expressed as

$$\mathbf{J}(r,m,k) = \delta(r - r_0)\mathbf{K}(m,k), \tag{56}$$

where, $\delta(x)$ is the Direc delta function, r_0 is the radius of the antenna, and the surface current density $\mathbf{K}$ is equal to[14]

$$\mathbf{K}(m,k) = \begin{Bmatrix} K_\theta \\ K_z \end{Bmatrix} = \begin{Bmatrix} -\dfrac{2}{\pi}I_0\dfrac{kL}{2m}\dfrac{\sin(kL/2 - m\pi/2)}{kL/2 - m\pi/2} \\ -\dfrac{m}{r_0 k}K_\theta \end{Bmatrix}. \tag{57}$$

where I_0 is the antenna current and L is the antenna length. The Fourier analysis transforms the antenna, which is an infinitesimally thin wire expressed as piecewise functions in physical domain, into a current sheet. For the annular configuration considered, $r_0 = a$ for the inner antenna and $r_0 = d$ for the outer antenna.

In general, the power transferred to the plasma, P_p, is expressed as

$$P_p = \frac{1}{2}\text{Re}\left(\int \mathbf{E}^* \cdot \mathbf{J}_{plasma} dV\right),$$ (58)

where $\mathbf{E}^*$ is the complex conjugate of the electric field and $\mathbf{J}_{plasma}$ is the current in plasma. In order to identify the dominant wave mode and wave number, it is useful to define spectral plasma power, P_s, so that

$$P_p = \sum_{m=-\infty}^{+\infty} \int_{k=-\infty}^{+\infty} P_s(m,k)dk \cdot$$ (59)

Substitution of Eq. (27) into Eq. (56) expresses the power as a function of $\mathbf{E}$ alone, i.e

$$P_s(m,k) = \frac{1}{2}\omega\varepsilon_0 \int_b^c \text{Im}\left[S\left(|E_r|^2 + |E_\theta|^2\right) + P|E_z|^2 + iD\left(E_\theta^* E_r - E_r^* E_\theta\right)\right]r\,dr \cdot$$ (60)

The spectral power can be also expressed in terms of wave velocity, ω/k. If helicon waves accelerate electrons to wave velocity through the Landau damping mechanism, then it is useful to express the power deposition as a function of electron energy. This yields[12]

$$P_e(m,\varepsilon_e) = \sqrt{\frac{m_e\omega^2}{8\varepsilon_e^3}}\left[P_s\left(m,\sqrt{\frac{m_e\omega^2}{2\varepsilon_e}}\right) + P_s\left(m,-\sqrt{\frac{m_e\omega^2}{2\varepsilon_e}}\right)\right],$$ (61)

where ε_e is electron energy. It is also useful to compute the radial power profile, P_r, which is expressed as

$$P_r(m,r) = \frac{1}{2}\omega\varepsilon_0 \int_{-\infty}^{+\infty}\text{Im}\left[S\left(|E_r|^2 + |E_\theta|^2\right) + P|E_z|^2 + iD\left(E_\theta^* E_r - E_r^* E_\theta\right)\right]dk \cdot$$ (62)

The radial power corresponds to the power absorbed by an infinitesimally thin shell of plasma with radius r.

III. Theoretical Analysis

Using the model described in Section II, the performance of an annular helicon source is investigated. The aim of this study is to characterize the relationship between the design parameters and the performance parameters. The design parameters considered in the study are the applied magnetic field strength and the antenna driving frequency. These parameters can be readily adjusted for a given geometry in an experiment by changing the frequency of the RF signal and the current through the solenoids. The performance parameters considered are the power deposited into plasma and wave velocity. If primary electrons are accelerated through Landau damping in helicon plasmas[5], the wave velocity should be selected such that the accelerated electrons have energy at which the ionization cross section with desired ion species is maximized. Unless otherwise noted, the study is based on the assumptions summarized in Table 1. The selection of the chamber radius, which is treated as a conducting surface, is arbitrary for the chamber radius

Table 1. Summary of Assumptions.

Geometric Parameters	
Inner Antenna Radius (a)	2.7 cm
Inner Plasma Boundary Radius (b)	3.0 cm
Outer Plasma Boundary Radius (c)	6.0 cm
Outer Antenna Radius (d)	6.3 cm
Chamber Radius (e)	20.0 cm
Plasma Properties	
Neutral Number Density	10^{20} m^{-3}
Electron Temperature	3 eV
Neutral Type	Argon
Antenna Parameters	
Antenna Type	Half Helical
Antenna Length	20 cm
Antenna Current	1 A

sufficiently larger than the outer antenna radius. The neutral density is fixed to 10^{20} m^{-3}, which is approximately 3.1 mTorr. The neutral density profile is assumed to be flat, whereas a parabolic density profile is assumed for plasma. However, the density at the boundary is set to 5% of the peak value to avoid the numerical singularity. Electron temperature of 3eV is used to compute the collisional cross section, but its pressure effect is neglected, as discussed in Section II.

For an annular helicon source, a pair of RF antennas are used to couple to the coaxial plasma column. The inner antenna is mounted inside of the inner tube and the outer antenna is mounted outside of the outer tube, so that the neither antenna is submerged in plasma. The inner and the outer antennas have the same twist rate. This allows the legs of the antennas to match azimuthally. Figure 2 shows an example of a pair of half helical antennas. The current in the twisted legs couple to the plasma; the end rings are there to complete the circuit. The analysis presented in this section assumes that the RF current through the legs of the inner and the outer antennas are in phase, unless otherwise noted.

Figure 2. A pair of half helical antennas.

A. Wave Mode

Helicon waves can be excited in either positive or negative m mode. For positive values of m, a stationary observer looking in the direction of the applied magnetic field sees the wave field rotate in the clockwise direction in time. For a negative wave mode, the field would rotate in the counter clockwise direction. The helicity of the wave is determined by the sign of m and the sign of the wave number k.[15] Experiments have shown poor coupling to negative m modes.[14,16] Figure 3 shows the spectral power loading for $m = 1$ and $m = -1$ modes. As the figure shows, the half helical antenna excites a wave of positive helicity, *i.e.* $m/k > 0$. The most dominant wave number for $m = 1$ and -1 modes are $k = 30$ m^{-1} and -26 m^{-1}, respectively. Note, for m = -1 case, the negative dominant value of k implies that the wave travels against the applied magnetic field. Thus, m = -1 is not

Figure 3. Spectral power loading for $m = 1$ and $m = -1$ modes at $n_0 = 2 \times 10^{18}$, f = 24 MHz, B_0 = 400 G.

suited as the ionization stage of a HET, as experiments have shown that peak plasma density is achieved a few wave length downstream of antenna location.[17] Reversing the direction of the applied magnetic field could solve the problem, but coupling the source to the HET acceleration stage is expected to become more difficult. For this particular configuration, the total power loading for $m = 1$ and $m = -1$ modes are 5.0 Ω and 3.7 Ω, respectively.

B. Antenna Frequency
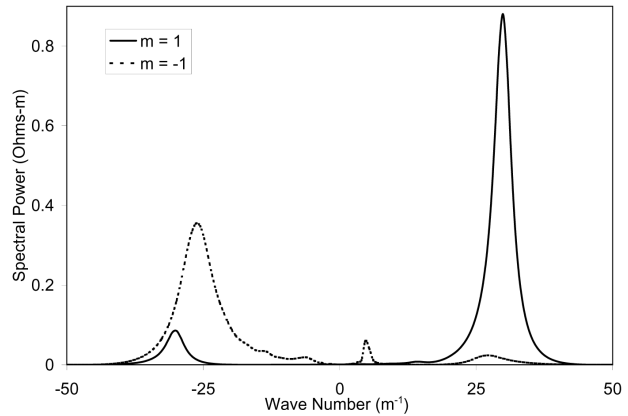
Antenna driving frequency is one of the parameters that can be adjusted for a given geometric configuration. The frequency affects both the location and magnitude of the peaks of the plasma power spectrum. In this analysis, the peak plasma density and the applied magnetic field strength are fixed to 2×10^{18} m^{-3} and 240 G, respectively. The plasma density and the applied magnetic field strength are in the range used previously for study of cylindrical helicon sources.[10,14,12] The antenna frequency is varied from 12 MHz to 44 MHz. Figure 4 shows the variation of plasma power loading computed using Eq. (59) and (60) as a function of frequency. As the figure shows, the power loading, which is the indicator of antenna coupling, varies significantly with the applied magnet field strength. The loading reaches approximately 3.1 Ω at frequency of 13 MHz and 44 MHz. The worst coupling of 0.85 Ω occurs at the frequency of approximately 29 MHz. Thus, for given peak plasma density and applied magnetic field strength, there exist a set of optimum antenna frequencies that maximize the antenna coupling.

In order to better understand the mechanism for the variation in the power loading, it is useful to analyze the power spectrum at different frequencies. Figure 5 shows the power spectrum at the frequencies of 28 MHz, which corresponds to the worst coupling, and 14 and 44 MHz, which correspond to the best coupling. At 14 MHz, the dominant wave number is approximately 29 m^{-1}. The corresponding wave velocity is approximately 3.0×10^6 m/s,
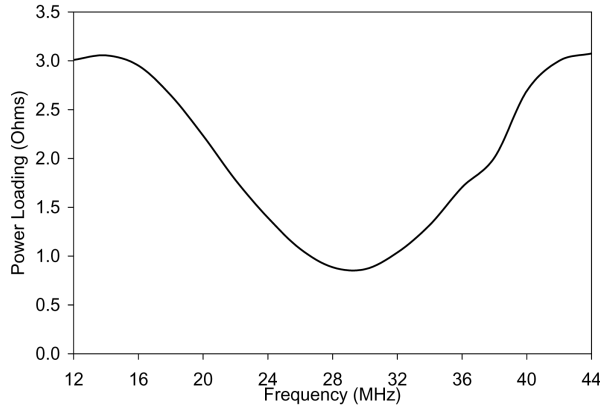
Figure 4. Variation of power loading as a function of the frequency at the peak plasma density of 2×10^{18} m^{-3} and applied magnetic field of 240 G.
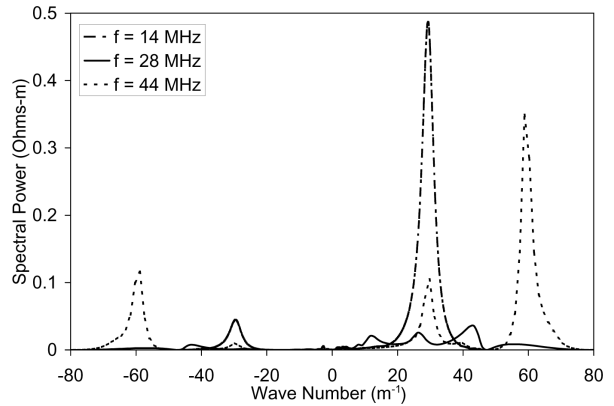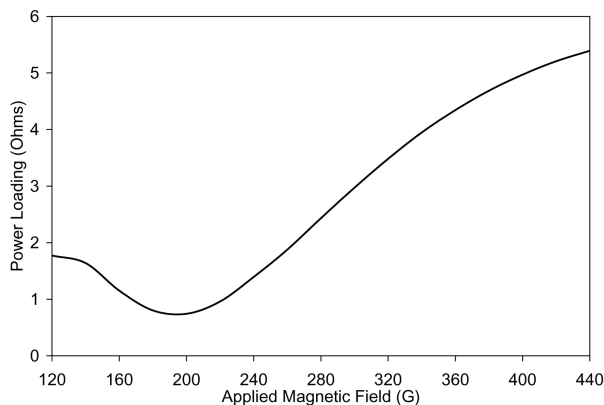

Figure 5. Spectral power loading at 14, 28, and 44 MHz at the peak plasma density of 2×10^{18} m^{-3} and applied magnetic field of 240 G.

and, if primary electrons are accelerated through Landau damping, the electron energy is 26.2 eV. At 44 MHz, the dominant wave number shifts to approximately 60 m^{-1}. Thus, compared to the 14 MHz case, the wave number of the dominant mode is doubled. These two wave numbers correspond to two different radial wave modes. The magnetic field structures of these two modes are discussed in details in Section E. The existence of different radial field patterns for cylindrical helicon sources has been considered using a simple helicon theory and observed experimentally for cylindrical helicon sources.[18] Although the frequency of 44 MHz is more than three time greater than 14 MHz, the wave velocity is only 1.5 times faster due to the larger dominant wave number of 44 MHz case. The primary electrons accelerated through Landau damping would have energy of 60 eV. Thus, assuming the electrons are accelerated through Landau damping, it is possible to adjust the frequency to accelerate the electrons to maximize the ionization cross section while maintaining high antenna coupling. However, if the frequency alone is adjusted, the selections of wave velocities that result in high antenna coupling are discrete. The power spectrum of the 28 MHz case, which results in the worst power coupling, shows several much smaller peaks. At this frequency, the wave field pattern switches from one mode to another, and the antennas couple poorly to either mode, resulting in a low power loading.

C. Applied Magnetic Field

The applied magnetic field strength is another parameter that can be adjusted for a given geometric configuration by adjusting the current through the solenoids. For this analysis, the plasma peak density and the antenna frequency are fixed to 2×10^{18} m^{-3} and 24 MHz. Figure 6 shows the variation of the power loading as a function of the applied magnetic field strength, varying from 120 G to 440 G. Similar to the variation of the power loading with the frequency, the graph shows two peak antenna couplings at 120 G and 440 G, and the worst coupling at 190 G.

Figure 6. Variation of power loading as a function of the applied magnetic field strength at the peak plasma density of 2×10^{18} m^{-3} and frequency of 24 MHz.
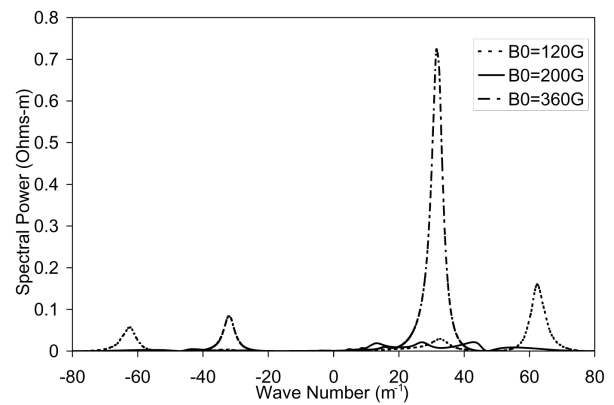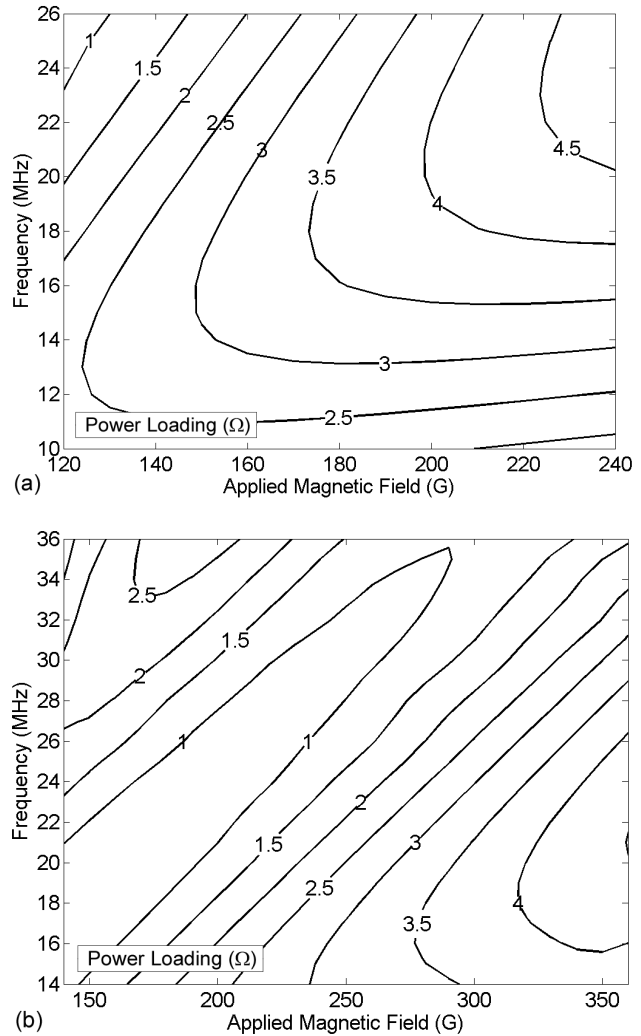

Figure 7. Spectral power loading at 130, 200, and 360 G at the peak plasma density of 2×10^{18} m^{-3} and frequency of 24 MHz.

American Institute of Aeronautics and Astronautics

However, unlike the frequency case, the coupling at 440 G is much higher than at 120 G. Note, the higher coupling for the 440 G case is not due to a better plasma confinement, because the problem of discharge equilibrium is not considered in the model; in real plasma, a higher magnetic field strength is expected to provide a better plasma confinement, thus less radial loss. Figure 7 shows the power spectrum at three different magnetic field strengths. At an applied magnetic field of 120 G, the dominant peak appears at wave number of 62 m^{-3}. At 24 MHz, the corresponding wave velocity accelerates the primary electrons to 17 eV. At the higher magnetic field strength of 360 G, the dominant wave number shifts to 31 m^{-1}. Thus, the wave length of the dominant wave is doubled, and the wave accelerates the primary electrons to 67 eV through Landau damping. Similar to adjusting the frequency, it is possible to vary the energy of primary electrons to maximize the ionization cross section by changing the applied magnetic field strength, if the Landau damping mechanism exists. However, the choice of wave velocities is again discrete.

D. Antenna Coupling: Frequency-Applied Magnetic Field Relationship

In Section B and C, the variation of power loading, which is the indicator of antenna coupling, is discussed. The analyses show that the antenna coupling varies significantly with frequency as well as applied magnetic field strength. For designing helicon sources, it is useful to combine the two analyses and express the variation of power loading as a function of the applied magnetic field strength and the frequency as a contour map. Figure 8 shows the result of the computation for plasma peak density of 1×10^{18} m^{-3} and 2×10^{18} m^{-3}. For the peak density of 1×10^{18} m^{-3}, the magnetic field is varied from 120 G to 240 G, and the frequency is varied from 10 MHz to 26 MHz. Figure 8a shows that the higher applied magnetic field requires higher frequency for best coupling. For example, the best coupling is achieved at 12 MHz for 120 G, but the peak shifts to 24 MHz at 240 G. Thus, the ratio of frequency-to-magnetic field (f/B_0) of 0.1 MHz/G produces the ideal coupling for the peak density of 1×10^{18} m^{-3}. Along the line, a better coupling is achieved at higher applied magnetic field and frequency, with the peak loading of 4.8 Ω achieved at the magnetic field of 240 G and the frequency of 24 MHz.

Figure 4b shows the power loading contour computed at the plasma peak density of 2×10^{18}. The applied magnetic field is varied from 140 G to 360 G, and the frequency is varied from 14 MHz to 36 MHz. Note, the graph shown in Figure 4 is the vertical slice of the contour map at applied magnetic field strength of 240 G, and the graph shown in Figure 6 is the horizontal slice of the contour map at frequency of 24 MHz. There are two ratios of frequency-to-applied magnetic field strength that results in high antenna coupling. These peaks excite two different radial wave modes. The first ratio of frequency-to-applied magnetic field is the ratio of 0.06 MHz/G, which corresponds to the first peak of

(a)

(b)

Figure 8. Contour of constant plasma power loading (Ω) as a function of applied magnetic field strength and antenna frequency at plasma density of (a) 10^{18} m^{-3} and (b) 2×10^{18} m^{-3}.

Figure 4 and the second peak of Figure 6. The second ratio is approximately 0.2 MHz/G, which corresponds to the second peak of Figure 4 and the first peak of Figure 6. Within the range of parameters considered in this analysis,

the peak coupling of 4.5 Ω is achieved for applied magnetic field strength of 360 G and frequency of 21 MHz. However, as shown in Figure 6, much higher power loading is achievable with a stronger applied magnetic field.

E. Radial Mode Shapes

Figure 9 compares two radial modes that exhibit high antenna loading at the plasma peak density of 2×10^{18} m^{-3}. The magnetic field structure for Mode 1, with $f/B_0 \approx 0.06$ MHz/G, is represented by the solid lines. Two configurations selected to represent Mode 1 are $B_0 = 360$G, $f = 20$ MHz and $B_0 = 440$ G, $f = 26$ MHz cases. Mode 2, $f/B_0 \approx 0.2$ MHz/G, is represented by dashed lines. The field structures for Mode 2 are represented by $B_0 = 120$ G, f = 24 MHz and $B_0 = 160$ G, f = 32 MHz cases. Note, for a fixed ratio of frequency-to-applied magnetic field, the
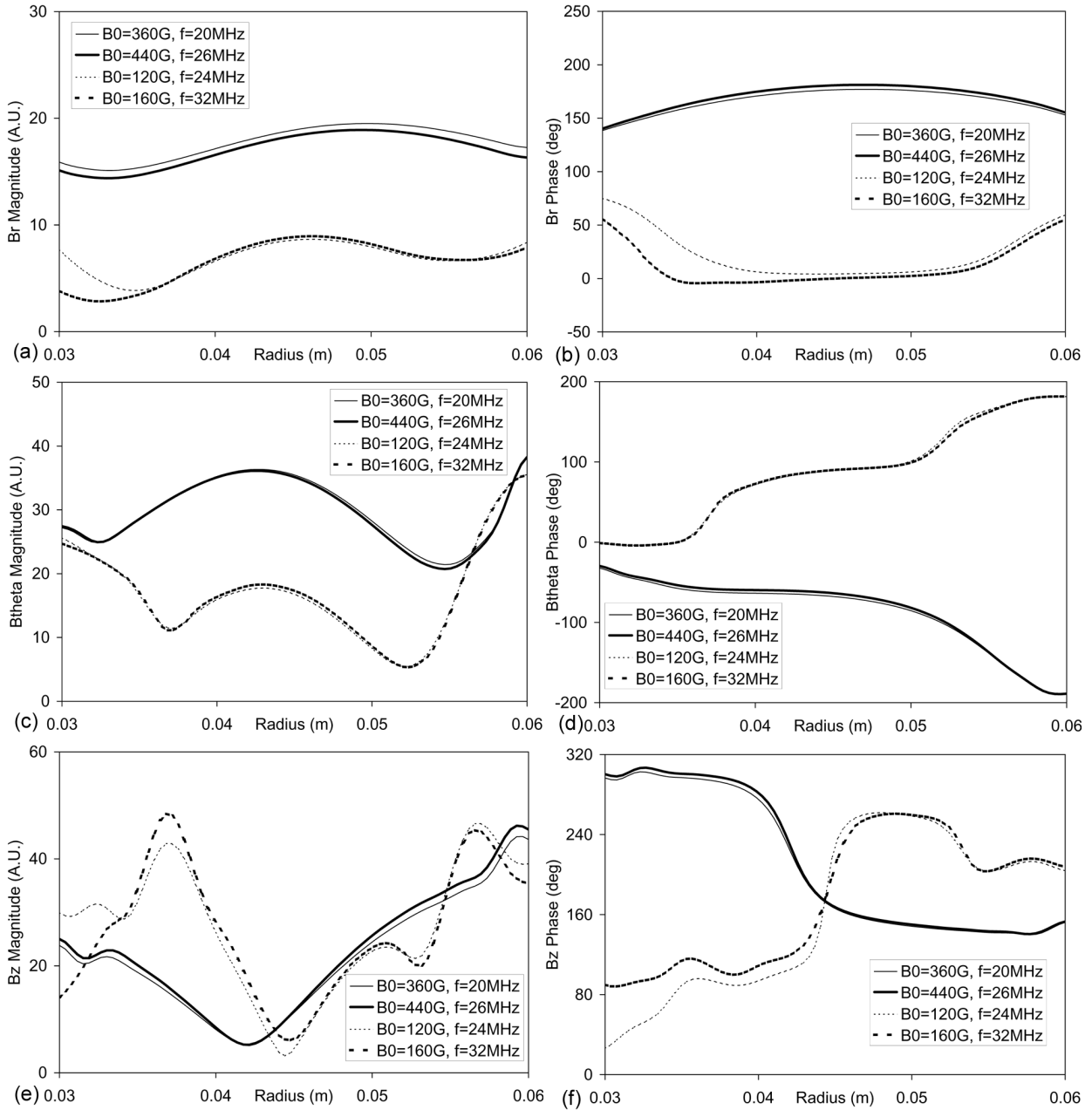
Figure 9. Comparison of the magnetic field for two different radial modes. The solid and dashed lines are the typical magnetic fields structures for $f/B_0 = 0.06$ MHz and $f/B_0 = 0.2$ MHz, respectively. Six plots shown are magnitude and phase of radial magnetic field (a, b), azimuthal magnetic field (c, d), and axial magnetic field (e, f).

magnetic field shapes are very similar. Figures 9a and 9c show that the variation of radial and azimuthal magnetic field magnitude are qualitatively similar for all four cases; all four cases exhibit peaks and troughs at approximately the same radial locations. The higher magnetic field amplitude for Mode 1 is simply due to better antenna coupling for the cases selected, *i.e.* the antenna loading for Mode 1 cases are 4.5 and 5.4 Ω, whereas the antenna loading for Mode 2 case are 1.8 and 2.4 Ω. On the other hand, Fig. 9b shows that the radial magnetic field of Mode 1 and Mode 2 have approximately 180° phase difference in the body of plasma. The phase of the azimuthal magnetic field gradually decreases from -30° to -190° for Mode 1, whereas the phase increases from 0° to 180° for Mode 2. In particular, the phases differ by approximately 180° near the center of the channel. Thus, the 180° phase difference of both radial and azimuthal magnetic field for Mode 1 and Mode 2 suggests that the magnetic field vectors pointing in nearly opposite directions in *r-θ* plane. Figure 9f shows the phase of the axial magnetic fields are also differs considerably for Mode 1 and Mode 2.

F. Antenna Current Configuration

An antenna parameter that is unique to an annular configuration is the choice of antenna current directions. The RF current through the legs of the inner and outer antennas can be in phase (parallel) or 180° out of phase (anti-parallel). The fields are established instantaneously in the model. Note, even in experiments, the difference in the inner and outer antenna path lengths has negligible effect on the antenna field, as the antenna field is established almost instantaneously due to a much greater wavelength of the RF signal compared to the antenna path lengths. In order to evaluate the antenna coupling in parallel and anti-parallel configurations, the power loadings for these two cases are compared. The peak plasma density is fixed to 2×10^{18} m^{-3} for both cases. Figure 10a shows variation of the power loading as a function of applied magnetic field strength and the antenna frequency for the anti-parallel case. The power loading for the parallel case is presented in Figure 8. The ratio of frequency-to-applied magnetic field that results in the best coupling is approximately 0.16 MHz/G for the anti-parallel case. The other ratio that produces a good coupling is 0.05 MHz/G. Note, these two ratios are slightly lower than the ratios for the parallel configuration, which are approximately 0.2 MHz/G and 0.06 MHz/G. Figure 10b shows the ratio of the power loadings for the parallel case and anti-parallel case. The ratio varies from 0.67 to 2.51. For most of the cases, the parallel configuration provides better antenna coupling. Note, the ratio of the power loadings is nearly constant for a given ratio of frequency to applied magnetic field strength.
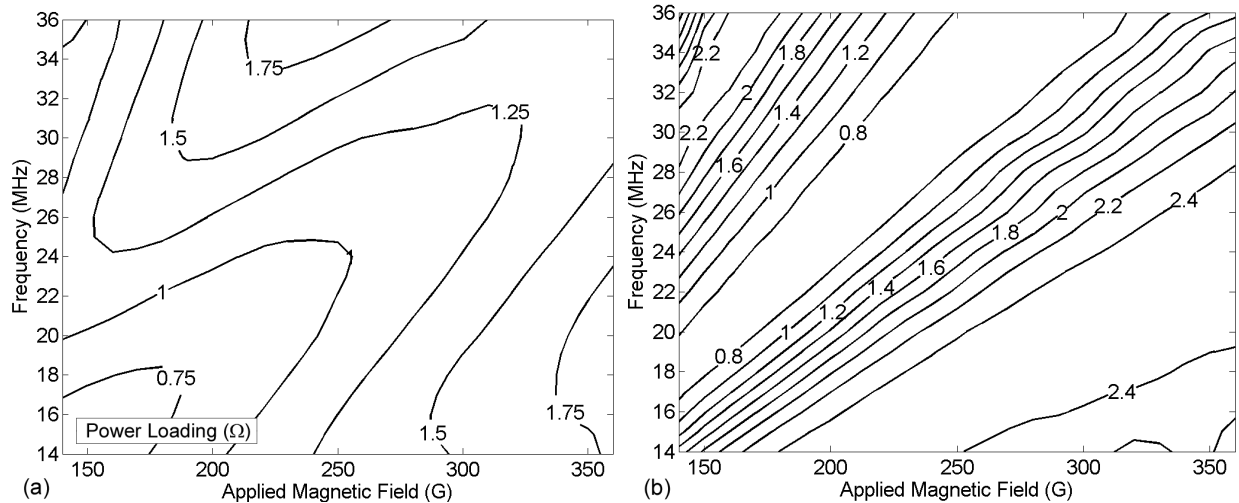
Figure 10. Contour of constant plasma power loading (Ω) as a function of applied magnetic field strength and antenna frequency at plasma density of (a) 10^{18} m^{-3} and (b) 2×10^{18} m^{-3}.

G. Density - Magnetic Field Relationship

The contour plot of constant power loading as a function of density and applied magnetic field at 20 MHz is shown in Fig. 11. The density varies from 5×10^{17} m^{-3} to 2.25×10^{18} m^{-3}, and the applied magnetic field varies from 100 to 400 G. The figure shows that the power loading varies from 0.8 to 4.8 Ω. For a fixed frequency, the applied magnetic field strength required to achieve the best coupling increases with the density. The ratio of the plasma density-to-magnetic field that results in the best coupling is approximately 4×10^{15} m^{-3}/G for this particular geometry

and antenna frequency. Note, the contour lines are approximately linear for most of the regions except near the region of peak coupling. Thus, increasing the magnetic field strength increases the plasma density if the power loading is fixed. This is similar to the result derived from simple helicon theory in which the plasma density varies linearly with the applied magnetic field strength in order to hold the total wave number constant.[1,8] The linear increase of the density with magnetic field has also been confirmed experimentally for cylindrical sources.[19] Along the line of best antenna coupling, a higher power loading is achieved at higher density and applied magnetic field. Experimentally, the increase in the plasma density with the input power has been observed for cylindrical helicon sources.[18]

H. Wave Velocity

There has been some speculation that high efficiency of helicon sources is due to the primary electrons acceleration to the wave velocity through the Landau damping mechanism.[5] Thus, it is useful to characterize the wave velocity in terms of the energy that the primary electrons have if the Landau damping mechanism exists. Furthermore, it is also useful to quantify the width of the electron energy distribution of such non-Maxwellian distribution. For this analysis, the width is defined as a point where the plasma spectral power drops to half of the peak value. Figure 12 shows the variation of the dominant primary electron energy as a function of the applied magnetic field strength and the frequency at the plasma peak densities of 1×10^{18} and 2×10^{18} m^{-3}. At the peak plasma density of 1×10^{18} m^{-3}, a higher frequency and applied magnetic field generally increases the dominant wave velocity. The 2×10^{18} m^{-3} case shows a similar behavior; however, the dominant peak jumps along the line of 0.122 MHz/G. Note, this corresponds to the transition in the dominant radial wave mode, which can also be inferred from the poor antenna coupling depicted in Fig. 8. Figure 13 shows the variation in the width of electron energy distribution function, assuming the Landau damping mechanism exists in helicon sources. At 1×10^{18}, the distribution width is primarily governed by the applied magnetic field strength. Thus, it is possible to alter the sharpness of the electron energy distribution function for a given distribution peak location. For example, both f = 15 MHz, B_0 = 240 G and f = 26 MHz, B_0 = 157 G results in the same peak location of approximately 50 eV, but the former has the distribution width of 26 eV whereas the latter has the width of 13 eV. At 2×10^{18}, a similar behavior is observed, although the width increases considerably when the dominant peak jumps.
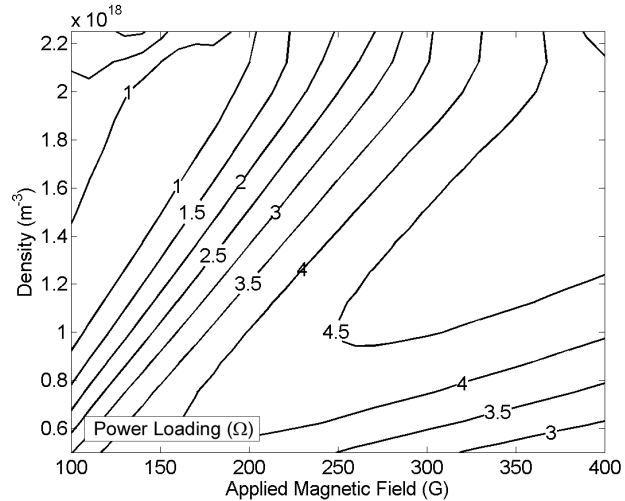
Figure 11. Contour of constant power loading (Ω) as a function of applied magnetic field and plasma density at the antenna frequency of 20 MHz.
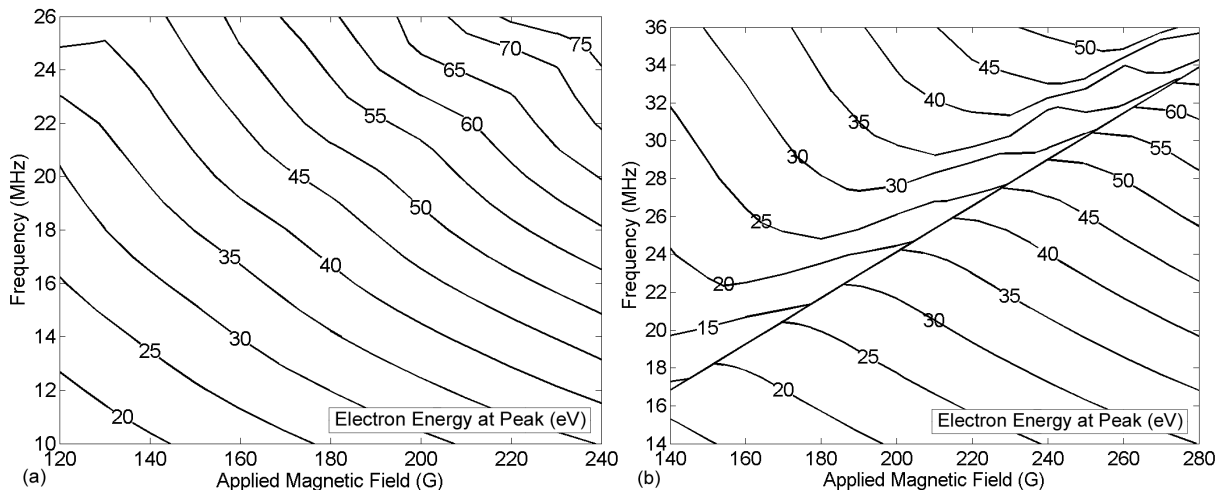
Figure 12. Contour of the peak electron energy (eV) as a function of applied magnetic field strength and the antenna frequency at plasma peak density of 10^{18} m^{-3} (a) and 2×10^{18} m^{-3} (b).
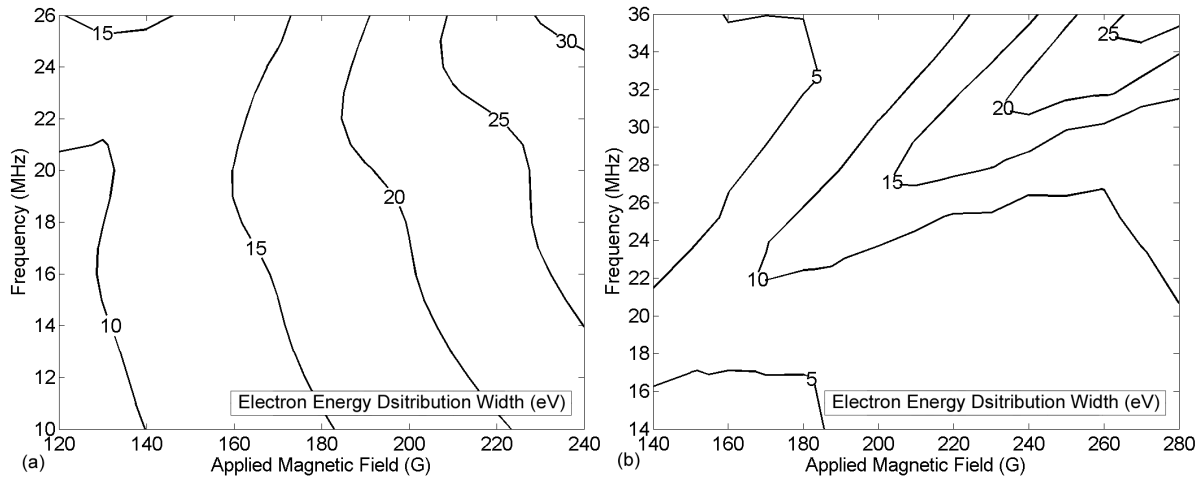
Figure 13. Contour of the electron energy distribution width (eV) as a function of applied magnetic field strength and the antenna frequency at plasma peak density of 10^{18} m^{-3} (a) and 2×10^{18} m^{-3} (b).

## IV. Experimental Apparatus

A. Vacuum Chamber

All experiments are conducted in the Vacuum Test Facility (VTF). The VTF is a stainless steel vacuum chamber that has a diameter of 4 m and a length of 7 m. The VTF pumping speed is varied by changing the number of diffusion pumps in operation. The combined pumping speed of the facility is 600,000 l/s on air and with a base pressure of 6.7×10^{-5} Pa (5×10^{-7} Torr).

B. Annular Helicon Plasma Source

Figure 14 shows the annular helicon plasma source used in this experiment. The annular ionization chamber is comprised of two concentric Pyrex tubes with inner diameters of 120 mm and 171 mm. A helical pitch antenna is wrapped on the outside of the outer tube, with a separate helical pitch antenna wrapped on the inside of the inner tube. The antennas are constructed from 1/2" wide by 1/8" thick copper strips, and are wrapped in 3M glass cloth electrical tape to prevent any local ionization outside the ionization chamber. RF power is provided to each antenna in-phase via the RF power system. Figure 15 shows a schematic of the complete RF power system.
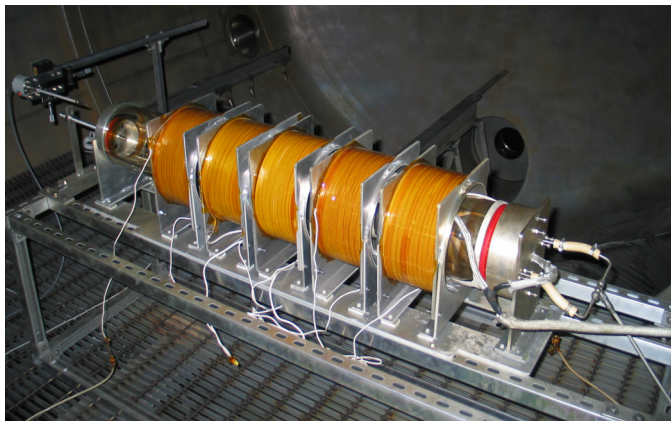
Figure 14. Annular helicon plasma source in the VTF.
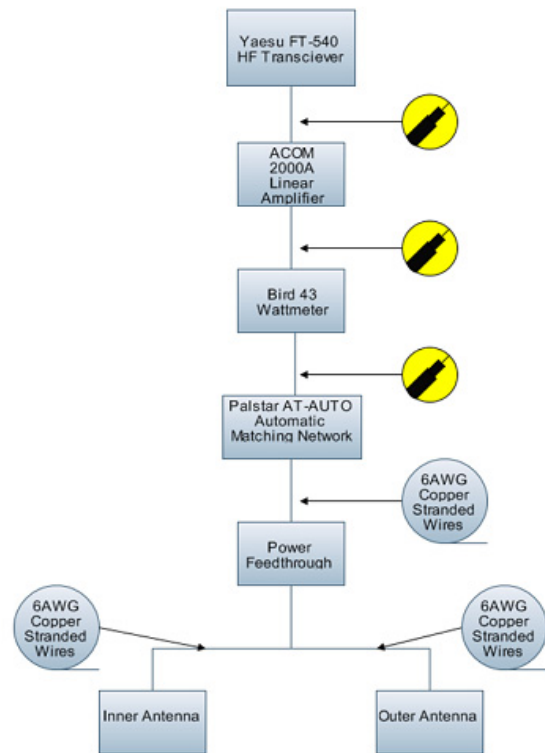
Figure 15. Schematic of the RF Power System

16
American Institute of Aeronautics and Astronautics

The annular helicon requires power for the inner and outer antennas as well as to the magnet solenoids. The RF power input leads connect at the downstream end of each helical antenna and the return leads connect at the anode end. The antennas carry current in the same direction. The antennas are aligned such that the legs twist on top of one another, which allows for optimal coupling of the antennas to the plasma. Five solenoids, powered by a 60-kW EMHP DC power supply, generate a steady-state axial magnetic field up to 450 Gauss. The power leads to the antennas and solenoids are EMF shielded with tinned copper mesh to eliminate RF radiation into and out of the wiring. Ferrites suppress RF signal propagation up the leads

The AT-Auto automatic matching network, which has a native impedance of 50 Ω, matches the impedance of the antenna system to the load. The impedance of the antennas is purely resistive, meaning no inductive reactance is present, and is extremely low. For this antenna configuration, the resistance is approximately 8 ohms without plasma present. To minimize radiation outside of the antenna and ionization channel, *i.e.*, reduce reflected and radiated power, the impedance of all cabling and feedthroughs is nearly 50 Ω. In addition, a standard fixed distance is maintained between all conductors.

High purity (99.9995% pure) argon gas is fed through an MKS 1179JA mass flow controller through stainless steel feed lines to the anode. A custom fixed volume mass flow calibration system is employed to ensure proper flow rates from the mass flow controller. The mass flow controller has an accuracy of ±1% of full scale.

C. RF-Compensated Langmuir probe

A Hiden Analytical systems ESPION Advanced RF-Compensated Langmuir probe is used for all electron number density and electron temperature measurements. Previous studies show that the ESPION system is a reliable diagnostic for measurements in RF plasmas.[20] The probe filament is a 0.15 mm diameter by 10 mm long tungsten wire. A reference electrode is position behind the filament. The probe filament is mounted to the end of a 316.5 mm long ceramic probe sting, which contains the required RF-compensation inductors. The Hiden software, connected to the control head, collects I-V curves from the plasma. The software package can use Orbital Motion Limited theory or the cold ion approximation of Allen, Boyd, and Reynolds to calculate the electron number density and electron temperature. The raw data may also be downloaded from the software and analyzed with thin sheath theory. The diagnostic has an accuracy of ±30%.[21]

V.   Operation of Plasma Source

A. Operational Regime

The annular helicon plasma source has been operated at RF frequencies of 6-15 MHz, including each second harmonic (up to 26 MHz), at power ranges of 50 W to 1 kW, for magnetic fields strengths of 0 to 450 Gauss, and argon flow rates of 15 to 100 sccm. Steady-state operation up to four hours has been demonstrated. To date, the qualitatively best inductively-coupled plasma to be generated occurred at a frequency of 7 MHz, 500 W, with a magnetic field of 150 Gauss. Initial measurements indicate electron number densities of 10^{17} m^{-3}. Figure 16 shows the qualitatively optimum case over the limited operating regime.
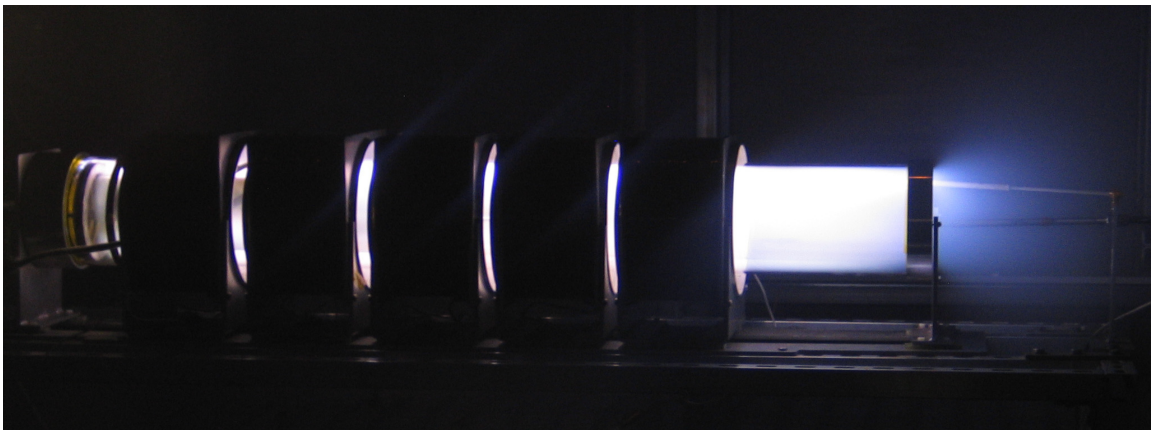
Figure 16. Optimal annular helicon plasma generation to date. Note the Langmuir probe positioned in the exhaust.

VI. Conclusion

A derivation of an annular helicon plasma source model, which considers the effect of both the helicon and TG wave, was presented. The model was used to analyze the behavior of a plasma source, with emphasis on power absorption. The effect of the antenna configuration, frequency selection, applied magnetic field strength, and plasma number density on antenna coupling was discussed. The ratio of frequency-to-applied magnetic field strength that results in an optimum antenna coupling for a given plasma density has been identified. By changing the frequency and the applied magnetic field strength, it is possible to adjust the wave velocity such that the primary electrions accelerated through Landau damping would have energy that maximizes the ionization cross section. The relationship between the density and applied magnetic field strength showed that there is an optimum magnetic field that maximizes the antenna coupling for a given density. The experimental work is currently in progress, which aims to verify the theoretical results in near future.

Acknowledgments

References

[1] R. R. Hofer, R. S. Jankovsky, "A Hall Thruster Performance Model Incorporating the Effect of a Multi-Charged Plasma," AIAA-2001-3322, *37th Joint Propulsion Conference and Exhibit*, Salt Lake City, UT, July 8-11, 2001.

[2] B. E. Beal, A. D. Gallimore, D. P. Morris, C. Davis, K. M. Lemmer, "Development of an Annular Helicon Source for Electric Propulsion Applications," AIAA 2006-4841, *42nd Joint Propulsion Conference and Exhibit*, Sacramento, CA, 2006.

[3] R. R. Hofer, P. Y. Peterson, A. D. Gallimore, "A High Specific Impulse Two-Stage Hall Thruster with Plasma Lens Focusing," IEPC-01-036, *27th International Electric Propulsion Conference*, Pasadena, CA, October 15-19, 2001.

[4] R. S. Jankovsky, D. T. Jacobson, V. K. Rawlin, et. al, "NASA's Hall Thruster Program," AIAA-2001-3888, *37th Joint Propulsion Conference and Exhibit*, Salt Lake City, UT, July 8-11, 2001.

[5] F. F. Chen, "Plasma Ionization by Helicon Waves," *Plasma Physics and Controlled Fusion*, Vol. 33, No. 4, 1991, pp. 339-364.

[6] R. W. Boswell, "Very Efficient Plasma Generation by Whistler Waves Near the Lower Hybrid Frequency," *Plasma Physics and Controlled Fusion*, Vol. 26, No. 10, 1984, pp. 1147-1162.

[7] V. V. Zhurin, H. R. Kaufman, R. S. Robinson, "Physics of Closed Drift Thrusters," *Plasma Sources, Science and Technology*, Vol. 8, No. 1, 1999, pp. R1-20.

[8] M. Yano, M. Walker, "Plasma Ionization by Annularly-Bounded Helicon Waves," *Physics of Plasmas*, Vol. 13, No. 6, 2006, pp. 063501-1-5.

[9] M. Yano, M. Walker, "Generalized Theory of Annularly-Bounded Helicon Waves," *Physics of Plasmas*, Vol. 14, No. 3, 2007, pp. 033510-1-7.

[10] F. F. Chen, D. Arnush, "Generalized theory of helicon waves. I. Normal modes," *Physics of Plasmas*, Vol. 4, No. 9, 1997, pp. 3411-3421.

[11] F. F. Chen, *Introduction to Plasma Physics and Controlled Fusion*, Plenum Press, New York, 1984, Appendix B.

[12] D. Arnush, "The Role of Trivelpiece-Gould Waves in Antenna Coupling to Helicon Waves," *Physics of Plasmas*, Vol. 7, No. 7, 2000, pp. 3042-3050.

[13] R. G. Jahn, *Physics of Electric Propulsion*, McGraw-Hill, New York, 1968, Chap 4.

[14] D. Arnush, F. F. Chen, "Generalized theory of helicon waves. II. Excitation and Absorption," *Physics of Plasmas*, Vol. 5, No. 5, May 1998, pp. 1239-1254.

[15] D. G. Mijak, F. F. Chen, "Helicon wave excitation with rotating antenna fields," *Plasma Sources, Science and Technology*, Vol. 7, No.1, 1998, pp. 61-74.

[16] D. D. Blackwell, F. F. Chen, "Two Dimensional Imaging of a Helicon Discharge," *Plasma Sources, Science and Technology,* Vol. 6, No. 4, 1997, pp. 569-576.

[17] M. Light, I. D. Sudit, F. F. Chen, D. Arnush, "Axial Propagation of Helicon Waves," *Physics of Plasmas*, Vol. 2, No. 11, 1995, pp. 4094-4103.

[18] J. P. Rayner, A. D. Cheetham, "Helicon Modes in a Cylindrical Plasma Source," *Plasma Sources, Science and Technology*, Vol. 8, No. 1, 1999, pp. 79-87.

[19] F. F. Chen, "Experiments on Helicon Plasma Sources," *ournal of Vacuum Science & Technology*, Vol. 10, No. 4, 1992, pp. 1389-1401.

[20] F. F. Chen, H. Torreblanca, "Large-Area Helicon Plasma Source with Permanent Magnets," *Plasma Physics and Controlled Fusion*, Vol. 49, 2006, pp. A81-93.

[21] J. L. Rovey, M. L. R. Walker, A. D. Gallimore, P. Y. Peterson, "Magnetically Filtered Faraday Probe for Measuring the Ion Current Density Profile of a Hall Thruster," *Review of Scientific Instruments*, Vol. 77, No. 1, 2006, pp. 013503-1-8.